# Evaluation of the Assumptions in the Steady-State Tropical Cyclone Self-Stratified Outflow Using Three-Dimensional Convection-Allowing Simulations

DANDAN TAO,[a,b,c] KERRY EMANUEL,[d] FUQING ZHANG,[a,b,f] RICHARD ROTUNNO,[e] MICHAEL M. BELL,[c] AND ROBERT G. NYSTROM[a,b]

[a] *Department of Meteorology and Atmospheric Science, The Pennsylvania State University, University Park, Pennsylvania*
[b] *Center for Advanced Data Assimilation and Predictability Techniques, The Pennsylvania State University, University Park, Pennsylvania*
[c] *Department of Atmospheric Science, Colorado State University, Fort Collins, Colorado*
[d] *Program in Atmospheres, Oceans, and Climate, Massachusetts Institute of Technology, Cambridge, Massachusetts*
[e] *National Center for Atmospheric Research, Boulder, Colorado*

(Manuscript received 9 February 2019, in final form 28 May 2019)

ABSTRACT

The criteria and assumptions that were used to derive the steady-state tropical cyclone intensity and structure theory of Emanuel and Rotunno are assessed using three-dimensional convection-allowing simulations using the Weather Research and Forecasting Model. One real-data case of Hurricane Patricia (2015) and two idealized simulations with and without vertical wind shear are examined. In all three simulations, the gradient wind balance is valid in the inner-core region above the boundary layer. The angular momentum $M$ and saturation entropy surfaces $s^*$ near the top of the boundary layer, in the outflow region and along the angular momentum surface that passes the low-level radius of maximum wind $M_{\mathrm{RMW}}$ are nearly congruent, satisfying the criterion of slantwise moist neutrality in the vicinity of $M_{\mathrm{RMW}}$. The theoretically derived maximum wind magnitude above the boundary layer compares well with the simulated maximum tangential wind and gradient wind using the azimuthally averaged pressure field during the intensification and quasi-steady state of the simulated storms. The Richardson number analysis of the simulated storms shows that small Richardson number ($0 < \mathrm{Ri} \leq 1$) exists in the outflow region, related to both large local shear and small static stability. This criticality of the Richardson number indicates the existence of small-scale turbulence in the outflow region. We also show that the stratification of temperature along the $M$ surfaces at the outflow region for steady-state hurricanes is approximately applicable in these three-dimensional simulations, while the radial distribution of gradient wind is qualitatively comparable to the theoretical radial profiles. Some caveats regarding the theory are also discussed.

## 1. Introduction

The observed, nearly circular structure of mature tropical cyclones (TC) has motivated the development of the axisymmetric TC theory. Further assumptions of hydrostatic and gradient wind balance in the free atmosphere above the TC boundary layer are supported by a scale analysis of the momentum and continuity equations (Willoughby 1979). In a series of papers, Emanuel (1986, 1997) developed a theory for steady-state TC's assuming hydrostatic and gradient wind balance above the boundary layer along with moist neutrality on constant absolute angular momentum ($M$) surfaces in the TC's inner core. In this potential intensity theory, the maximum gradient wind speed at the top of the boundary layer is related to the temperature difference between the boundary layer and outflow as well as the gradient of saturation entropy $s^*$ across $M$ surfaces. This theory also assumes that the streamlines emerging from the boundary layer all converge to a constant absolute temperature at the tropopause. However, Emanuel and Rotunno (2011, hereafter ER11) pointed out that the assumption of constant outflow temperature is not consistent with the results of numerically simulated tropical cyclones in which the temperature in the outflow region increases rapidly

Denotes content that is immediately available upon publication as open access.

[f] Deceased.

*Corresponding author*: Kerry Emanuel, emanuel@mit.edu

DOI: 10.1175/JAS-D-19-0033.1

with $M$. In their revised theory (ER11; Emanuel 2012, hereafter E12), they proposed that the absolute temperature in the outflow region is not a constant, and that its stratification is determined by small-scale turbulence that limits the gradient Richardson number (Ri) to be near a critical value ($\mathrm{Ri}_c$). Following these assumptions, they derived an equation for the outflow temperature as a function of $M$:

$$\frac{\partial T_o}{\partial M} \cong -\frac{\mathrm{Ri}_c}{r_t^2}\left(\frac{dM}{ds*}\right), \tag{1}$$

where $T_o$ is the outflow temperature, $\mathrm{Ri}_c$ is the critical Richardson number, and $r_t$ is some physical radius in the outflow region. In ER11 and E12, this equation serves as an upper boundary condition for the derivation of the balanced gradient wind radial profile in the TC's inner core above the boundary layer.

The Richardson number is the square of the ratio of the buoyancy frequency to the local vertical wind shear. Linear theory and laboratory experiments show an onset of turbulence when the gradient Richardson number falls below a critical value ($\mathrm{Ri}_c = 0.25$). Given that current resolution of models can only be used to calculate bulk Richardson number, this critical value is extended to 1 ($\mathrm{Ri}_c = 1$), which is often used as a threshold for the occurrence of parameterized small-scale turbulent mixing processes in models. The occurrence of Ri criticality in real TCs has recently been studied by Molinari et al. (2014) and Duran and Molinari (2016), who found that the Ri is indeed small in the outflow region of observed tropical cyclones. Both studies showed that low values of the Richardson number are frequent at around 13.5-km height within about 200-km radius, and that the altitude of the lowest Ri steadily decreases with radius to a height of around 11.5 km at 1000 km away from the storm center. They attributed the frequent occurrence of low Ri in the upper troposphere to both small static stability and large local vertical wind shear. They also found that weaker TCs have less frequent occurrences of low Ri than hurricanes. These observational studies support the assumption of Ri criticality in the outflow region of steady-state TCs proposed by ER11.

The basic insight of ER11 is that the TC outflow stratification embodied in $\partial T_o/\partial M$ is created by the TC itself and not determined by the environment. The purpose of this paper is to validate the assumptions used in ER11, to evaluate the diagnostic equation for the maximum gradient wind speed at the top of the boundary layer and also to compare the radial profile of the tangential/gradient wind at the boundary layer top to the one from the ER11 self-stratification theory. Our evaluation of the ER11 assumptions uses three-dimensional simulations consisting of one real-world case of Hurricane Patricia (2015), one idealized case of development in a homogeneous environment and another idealized case of development in a moderately sheared flow. Section 2 describes the experimental setup. Section 3 provides the overview of the three cases. Section 4 presents the results of checking the assumptions and comparing the predicted maximum gradient winds and radial profiles to those extracted from the model simulations. Summary and discussion are provided in section 5.

## 2. Experimental setup

### a. *Deterministic forecast of Hurricane Patricia (2015) from the Pennsylvania State University real-time Hurricane Prediction System*

Hurricane Patricia (2015) is a historic storm that broke several records (Rogers et al. 2017). The simulation of Hurricane Patricia (2015) analyzed in this study is the deterministic forecast generated by the Pennsylvania State University (PSU) real-time Atlantic hurricane forecast and analysis system (F. Zhang et al. 2009, 2011; Zhang and Weng 2015; Weng and Zhang 2016). Here we are analyzing a model that was run in real time, not designing new simulations. The purpose of this real case is to test the agreement between the analytic theory and the real-case simulation in operational forecasts without further tuning. The simulation employed version 3.5.1 of the Weather Research and Forecasting (WRF) Model with an initial condition that included the assimilation of routine observations and airborne Doppler radar velocity, using the ensemble Kalman filter method developed by Zhang and Weng (2015).

Four two-way nested domains are utilized with horizontal grid spacings of 27, 9, 3, and 1 km, which contain 378 × 243 grid points for the outermost domain (D1) and 297 × 297 grid points for each of the inner three domains (D2–D4). There are 42 vertical model levels with the top level at 10 hPa (~30 km) and a vertical grid spacing of about 0.9 km between $z$ = 11–17 km. The simulation uses the Yonsei University (YSU) boundary layer scheme (Hong et al. 2006) to represent the vertical turbulent mixing. The horizontal diffusion is implicitly included (diff_opt = 0 in WRF) in the advection scheme. The surface fluxes of momentum and moist enthalpy are parameterized in terms of wind-dependent "exchange coefficients" $C_d$ and $C_k$, respectively, follows the recent study of Chen and Yu (2016) and Chen et al. (2018). A cumulus parameterization is used only for D1. The analysis in this paper is based on the simulation output from D4 with a 1-km horizontal grid spacing.

*b. Idealized simulations with high vertical resolutions*

The two idealized simulations were run using WRF, version 3.9. Though the idealized simulations here use a newer version of WRF than that of the real-case simulation, there is no documented change in the fundamental model physics or performance between these two versions. One of the idealized experiments has no background flow (NOFLOW), while the other experiment has 5 m s$^{-1}$ westerly environmental shear (SH5) between 200 and 850 hPa using a point downscaling method that introduces vertical wind shear in the simulation without a horizontal temperature gradient (Nolan 2011). The vertical profiles of the background flows are shown in Fig. 1 of Tao and Zhang (2014) that the shear is linear with height. The initial vortex is a modified Rankine vortex with a maximum surface wind speed of 15 m s$^{-1}$ at a 135-km radius. The domain is doubly periodic with a constant Coriolis parameter ($f = 5 \times 10^{-5}$ s$^{-1}$). The moist tropical sounding of Dunion (2011) is used to set up the thermodynamic environment, and both experiments have a constant sea surface temperature of 27°C. There are three two-way nested model domains, with domain sizes of 4320 km × 4320 km (D1), 1440 km × 1440 km (D2), and 720 km × 720 km (D3), and horizontal grid spacings of 18, 6, and 2 km, respectively. The model has 98 vertical levels with the model top at 24.5 km. The vertical grid spacing is around 0.3 km between $z$ = 10–15 km. The vertical resolution in the outflow region in the idealized simulations is about 3 times higher than that in the real-case simulations, which will influence the magnitude of local vertical wind shear and hence the Ri value (shown in section 4d). The Ri value is sensitive to vertical grid spacings ($dz$ = 0.3 km vs $dz$ = 0.9 km in the outflow region) while horizontal resolution has little influence on the Ri value ($dx$ = 1 km vs $dx$ = 3 km) according to the comparisons between the results from simulations with different horizontal and vertical resolutions (not shown). Nevertheless, the fundamental physics behind the simulations should not have been altered.

As with the Patricia simulation, these simulations use YSU boundary layer scheme, WRF single-moment 6-class microphysics scheme (WSM6) (Hong and Lim 2006). Different from the Patricia simulation, these idealized simulations use a simple horizontal diffusion option (diff_opt = 1 in WRF) with two-dimensional deformation (km_opt = 4 in WRF), no cumulus parameterization and no radiation schemes. The analysis of these idealized simulations in this paper is based on the simulation output from D3 with a 2-km horizontal grid spacing.

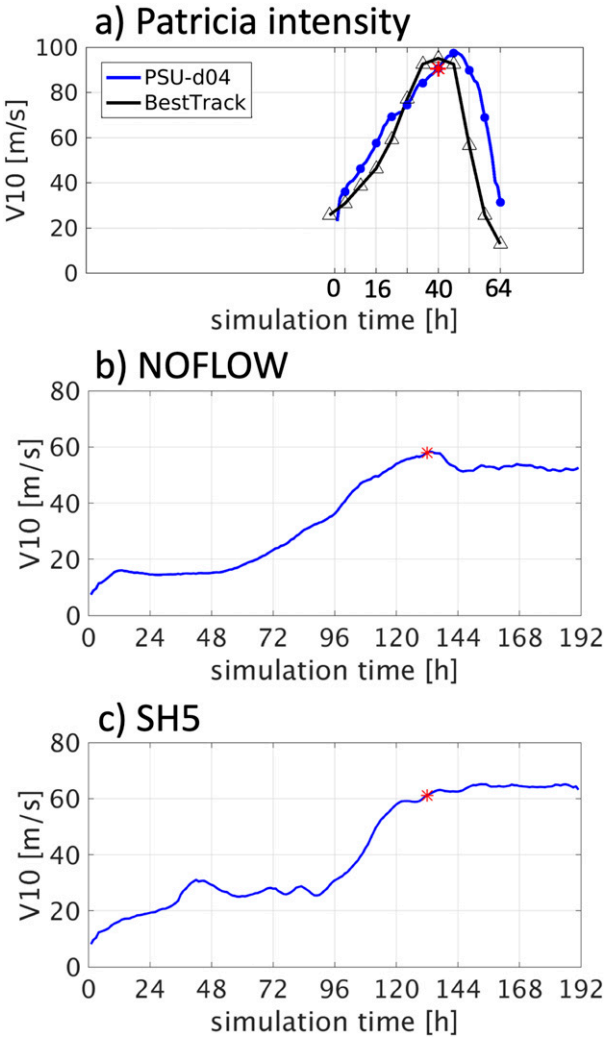


FIG. 1. Intensity evolution of (a) Patricia (blue dots and black triangles denote 6-h intervals), (b) NOFLOW, and (c) SH5. The red stars denote the times used for detailed analysis in subsequent figures.

## 3. Overview of the three simulations

The maximum 10-m total wind evolutions are shown in Fig. 1. The intensity from D4 of Hurricane Patricia (2015) simulation (PSU-d04) is reasonable compared to the best track data (Fig. 1a). The rapid intensification and weakening are well captured by the model as well as the extreme intensity of 95 m s$^{-1}$. The rapid weakening in Patricia's intensity after 46 h is mainly due to its landfall.

NOFLOW and SH5 are idealized simulations starting from a weak cyclone. NOFLOW intensifies from 54 to 136 h and weakens slightly due to a secondary eyewall formation afterward (not shown). The rapid intensification of SH5 starts at 90 h and ends at 122 h. The simulation reaches a quasi-steady state after the rapid

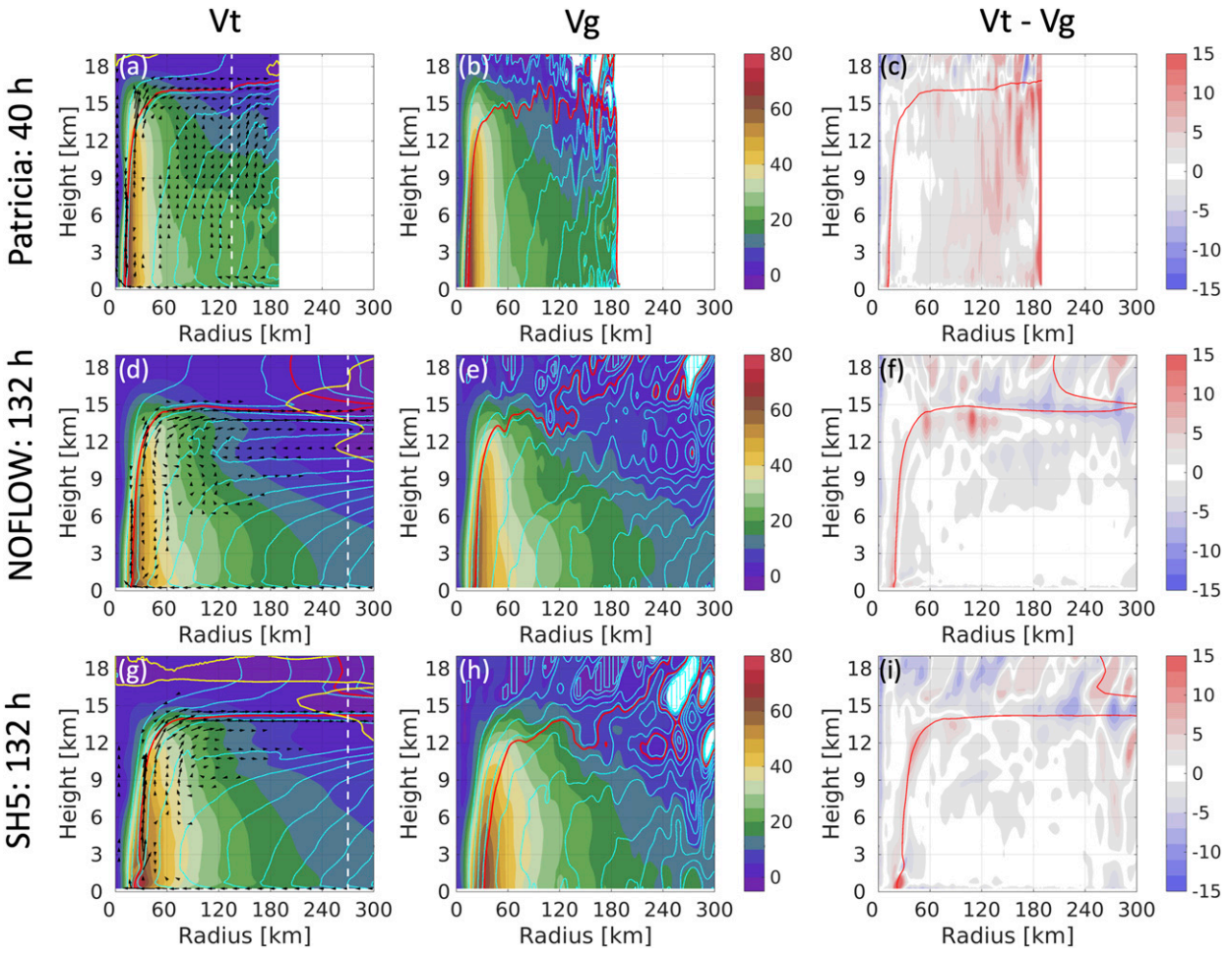


FIG. 2. (left) Azimuthally averaged tangential wind (shading; $V_t = 0\,\mathrm{m\,s^{-1}}$ is the orange contour), secondary circulation (black vectors; wind speed smaller than $2.5\,\mathrm{m\,s^{-1}}$ is not shown), and angular momentum (cyan contours with an interval of $0.5 \times 10^6\,\mathrm{m^2\,s^{-1}}$; $M_{\mathrm{RMW}}$ in red); white dash lines separate the area with full azimuth data (radius $\leq$ 135 km in Patricia and radius $\leq$ 270 km in NOFLOW and SH5) and the area with partial azimuth data (radius $>$ 135 km in Patricia and radius $>$ 270 km in NOFLOW and SH5). (center) Gradient wind calculated from azimuthally averaged pressure field and angular momentum calculated from gradient wind, (right) Difference between azimuthally averaged tangential wind and gradient wind. (a)–(c) Patricia at 40 h, (d)–(f) NOFLOW at 132 h, and (g)–(i) SH5 at 132 h.

intensification. The vortex structures of NOFLOW and SH5 at different stages are similar to their counterparts with a coarser vertical resolution (41 vertical levels) shown in Tao and Zhang (2019). NOFLOW has an axisymmetric structure at all times, while SH5 experiences episodes of strong asymmetry before the onset of rapid intensification (RI) but has persistently small asymmetry after RI onset.

We select the simulation results at 40 h (1200 UTC 23 September 2015) for Patricia and at 132 h for NOFLOW and SH5 as display times for sections 4a, 4b, and 4d–4f. The other times (Patricia: 20–40 h; NOFLOW and SH5: 120–180 h) give similar results for sections 4a, 4b, 4d, and 4e as the selected times and are not shown to avoid repetition. The maximum 10-m total wind speed of Patricia at 40 h is $92\,\mathrm{m\,s^{-1}}$, while the maximum 10-m total wind speeds of NOFLOW and SH5 at 132 h are 58 and $62\,\mathrm{m\,s^{-1}}$ respectively. NOFLOW has slightly weaker maximum intensity than SH5, which is associated with its secondary eyewall formation.

The left column of Fig. 2 shows the azimuthally averaged primary circulation and secondary circulation as well as the absolute angular momentum $M$ for the three simulations at the selected times. Patricia (Fig. 2a) has a compact primary circulation, with a surface radius of maximum azimuthally averaged tangential wind (RMW) of around 10 km. The $30\,\mathrm{m\,s^{-1}}$ contour extends only to a radius of 55 km. The $10\,\mathrm{m\,s^{-1}}$ contour reaches a height of 17 km, while the main outflow region is between $z = 15$ and 16.5 km. NOFLOW (Fig. 2d) has a slightly larger primary circulation compared to Patricia. The surface RMW is around 18 km with the $30\,\mathrm{m\,s^{-1}}$ wind contour

extending to a radius of 90 km. The main outflow region is located between $z$ = 13–15 km. SH5 (Fig. 2g) has the largest primary circulation among the three cases with a surface RMW of 22 km. The outflow height of SH5 is similar to NOFLOW.

The absolute angular momentum is defined as

$$M = rV_t + \frac{1}{2}fr^2, \tag{2}$$

where $r$ is the radius to the surface center, $V_t$ is the azimuthally averaged tangential wind calculated using the surface center, and $f$ is the Coriolis parameter. In Patricia, we simply use the $f$ value at Patricia's surface center for calculation. Though $f$ changes with latitude, this difference in calculating $M$ and even the entire second term of (2) are negligible in the TC's inner core. The $M$ surface that passes surface RMW (denoted as $M_{\mathrm{RMW}}$) follows the eyewall updrafts and then the outflow region. In this paper, the region of interest is along $M_{\mathrm{RMW}}$ and its vicinity. The $M_{\mathrm{RMW}}$ contour will act as a reference in the following sections.

## 4. Results

### a. Gradient wind balance

The maximum wind speed and radial profile derived from the ER11 theory are both dependent on the gradient winds $V_g$ at the boundary layer top. We first evaluate the assumption of gradient wind balance. Using the azimuthally averaged pressure field from the model output, the gradient wind is calculated and shown in the second column of Fig. 2. The difference field between $V_t$ and $V_g$ is shown in the third column of Fig. 2. When compared to the azimuthally averaged tangential wind from the model output, the gradient wind captures the structure and magnitude within the TC inner core (radius $<$ 100 km), above the boundary layer but below the outflow region. In the outflow region, there are areas confirming the existence of the violation of gradient wind balance as stated in Cohen et al. (2017). In the boundary layer, the supergradient jet is missing in the gradient wind calculation as expected. The magnitude of the maximum gradient wind inside the boundary layer is persistently smaller than the maximum tangential wind. In sections 4c and 4f, we use the altitudes where the maximum tangential winds first agree quantitatively with the maximum gradient winds as the heights of the boundary layer top, which are $z$ = 1.4 km for Patricia, $z$ = 1 km for NOFLOW, and $z$ = 1.5 km for SH5.

### b. Slantwise moist neutrality

The ER11 theory assumes slantwise moist neutrality, which implies that the saturation entropy $s^*$ is a function of absolute angular momentum $M$ alone [$s^* = s^*(M)$]. This assumption is checked in Fig. 3, in which the distributions of $s^*$ and $M$ are shown. The calculation of saturation entropy uses the same equation as (1) in ER11. From Figs. 3a–c, we find that $s^*$ maximizes in the lower eye region (~3-km height in Patricia, ~4.5-km height in NOFLOW and SH5). The congruent $M$ and $s^*$ surfaces are found in the lower boundary layer, the eyewall updrafts, and especially in the vast outflow region (Figs. 3b,d,f). Hence, $s^*(M)$ is approximately satisfied in these quasi-steady-state TCs following the eyewall updrafts and the connected outflow. The assumption of the slantwise moist neutrality is thus reasonable in the vicinity of $M_{\mathrm{RMW}}$. Outside the eyewall region, the $M$ surfaces are nearly orthogonal to $s^*$ surfaces in the lower troposphere above the boundary layer.

### c. Evaluation of the diagnostic maximum gradient wind speed equation

From hydrostatic and gradient balance as well as slantwise moist neutrality, the derived angular velocity equation at the top of the boundary layer is [(13) of E12]

$$V^2 = -(T_b - T_o)M\frac{ds^*}{dM}, \tag{3}$$

where $T_b$ is the temperature at the boundary layer top and $T_o$ is the outflow temperature where the tangential wind vanishes ($V_t = 0\,\mathrm{m\,s^{-1}}$). To do the calculation from the azimuthally averaged fields of the three numerical simulations, we use $T_b$ on $M_{\mathrm{RMW}}$ at the boundary layer top ($z$ = 1.4 km for Patricia, $z$ = 1 km for NOFLOW, and $z$ = 1.5 km for SH5). For $T_o$, we use the outflow temperature on the $M_{\mathrm{RMW}}$ at the location of $V_t = 0\,\mathrm{m\,s^{-1}}$ (NOFLOW and SH5) or at the radius that reaches the farthest edge of the domain (135 km for Patricia). Because of the congruence of $M$ and $s^*$ surfaces along $M_{\mathrm{RMW}}$, $ds^*/dM$ should be constant on the $M_{\mathrm{RMW}}$ surface above the boundary layer. To avoid the unwanted fluctuations and obtain a smoother $V$ evolution from (3), $ds^*/dM$ is calculated using the linear regression coefficient of $s^*$ against $M$ (Fig. 4) in the outflow region, which can be a good approximation to get $ds^*/dM$. But in the early stages of development, $s^*$ and $M$ surfaces are not well aligned even in the updraft region, as shown by Peng et al. (2018, 2019), which will lead to the poor results of $ds^*/dM$. To avoid imaginary values of $V$, we set $M(ds^*/dM)$ to zero wherever it is positive. The time-dependent values of $(T_b - T_o)$ and $M(ds^*/dM)$ as well as the diagnosed $V$ are shown in Fig. 5. Given the similar boundary layer top heights in Patricia and SH5, Patricia has a much larger temperature difference between the boundary layer top and the outflow region ($95 < T_b - T_o < 105$ K) than SH5 ($80 <$

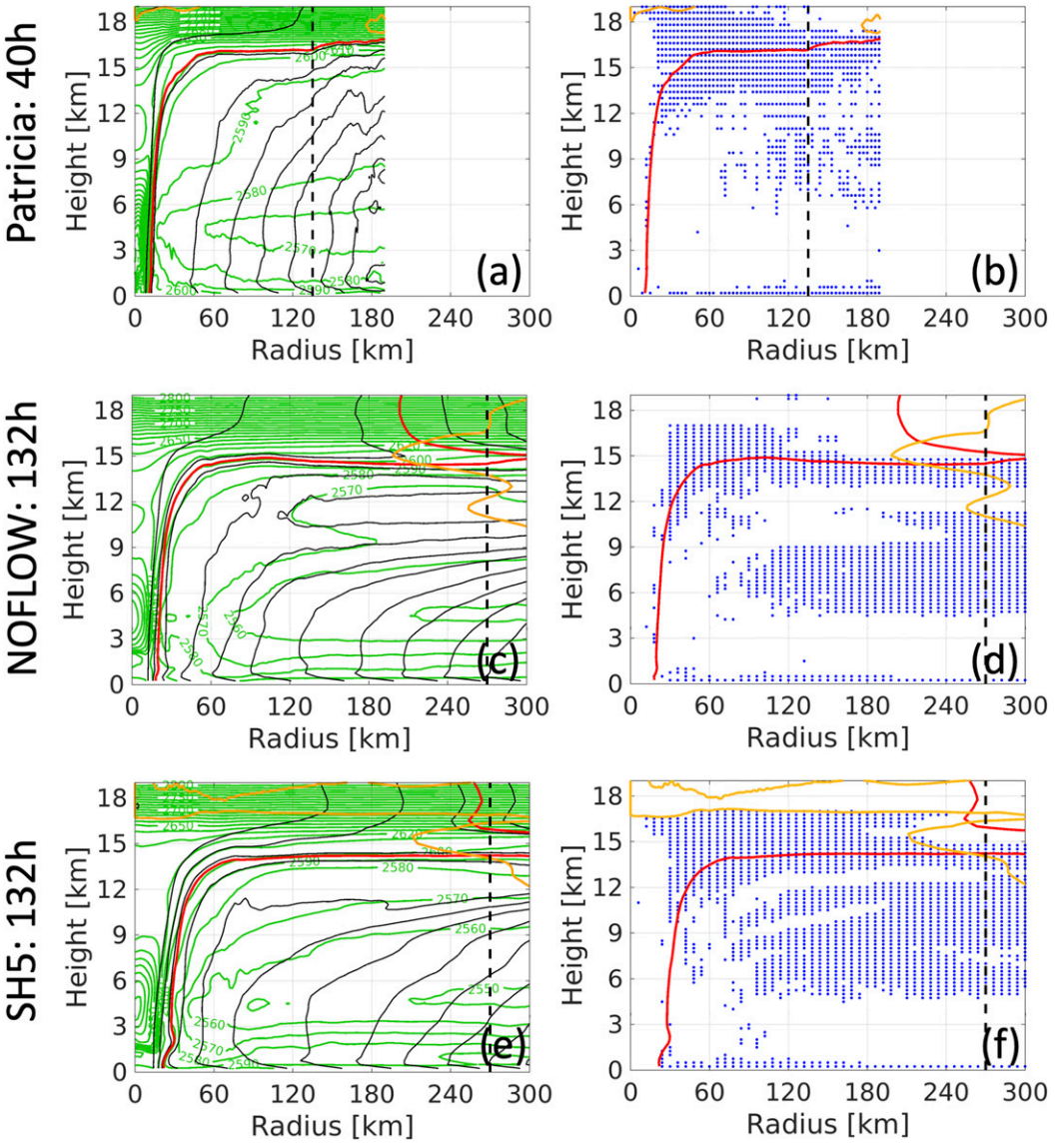


FIG. 3. (left) Profile of $s^*$ (green contours; J kg$^{-1}$ K$^{-1}$) and $M$ (black contours with an interval of $0.5 \times 10^6$ m$^2$ s$^{-1}$; $M_{\mathrm{RMW}}$ in red) fields. (right) Dots denote the location where the angle between $\nabla s^*$ and $\nabla M$ is within the range of 175°–185°. (a),(b) Patricia at 40 h, (c),(d) NOFLOW at 132 h, and (e),(f) SH5 at 132 h. Contours of $V_t = 0$ m s$^{-1}$ are orange. Black dash lines separate the area with full azimuthal data (radius ≤ 135 km in Patricia and radius ≤ 270 km in NOFLOW and SH5) and the area with partial azimuthal data (radius > 135 km in Patricia and radius > 270 km in NOFLOW and SH5).

$T_b - T_o < 85$ K) during the quasi-steady state. The reason for this difference can be explained in two ways: one is that Patricia has a much higher outflow region than SH5 (Figs. 2a,g); the other is that the tropopause temperature in Patricia is much lower than that in SH5 (will be shown in section 4e). The value of $(T_b - T_o)$ in NOFLOW is larger than SH5 mainly due to the lower boundary layer top. The time dependence of $(T_b - T_o)$ is mostly due to the increasing height of the outflow region during the intensification stage. However, the variance of $(T_b - T_o)$ contributes at most 15%[1] to the variance of $V$, which means the differences in $V$ are mainly attributable to the differences in $M(ds^*/dM)$. Figures 5b, 5e, and 5h show that, excluding the zeroed values near the beginning, $M(ds^*/dM)$ evolves from small values near 0 to $\sim -75$ m$^2$ s$^{-2}$ K$^{-1}$ in Patricia, to

[1] This number is simply calculated by $\max(\sqrt{(T_b - T_o)_{\max}/(T_b - T_o)_{\min}} - 1) \times 100\%$.

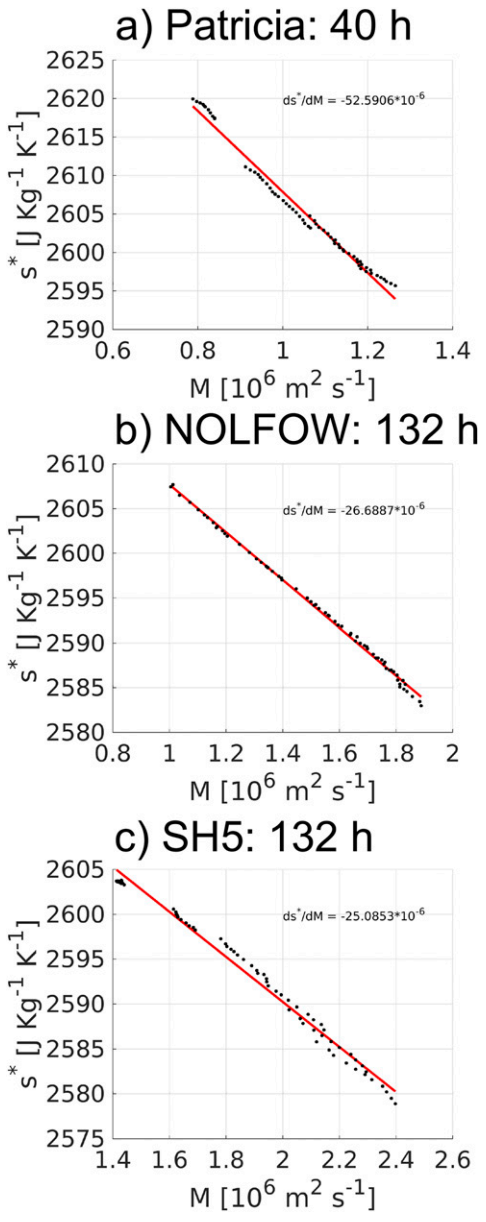


FIG. 4. Plots of $s^*$ against $M$. The data are from the regions (a) between 3RMW and 3RMW + 10 km and between 1200 m below and 800 m above $M_{\mathrm{RMW}}$ and (b),(c) between 3RMW and 3RMW + 10 km and between 750 m below and 500 m above $M_{\mathrm{RMW}}$. The coefficient from the linear regression is used to present the $ds^*/dM$ in $V$ equation.

$\sim -45\,\mathrm{m^2\,s^{-2}\,K^{-1}}$ in NOFLOW and $\sim -60\,\mathrm{m^2\,s^{-2}\,K^{-1}}$ in SH5. Most of the intensification stages are captured in $M(ds^*/dM)$. The time dependence of $M(ds^*/dM)$ mostly comes from the entropy and absolute angular momentum distributions in the boundary layer, which are highly related to the boundary layer dynamics as well as the surface exchange coefficients [it is not explicitly shown in (3); detailed derivation available in E12]. From the right column of Fig. 5, it is apparent that the diagnosed $V$ is quantitatively comparable to $V_t$ and $V_g$ in all three simulations at all times after the storm is well developed, except for the early stage of SH5 when SH5 still has large asymmetry before the RI onset due to the vertical wind shear (Tao and Zhang 2019).

### d. Richardson number distribution

The radial profile of the angular velocity at the boundary layer top in steady-state TCs developed in ER11 is about the role of small-scale turbulent mixing on setting the temperature stratification in the outflow region based on the critical Richardson number. When the Richardson number is smaller than this critical value, the flow is dynamically unstable and likely to initiate turbulent mixing. A classic way to parameterize the turbulence in numerical models uses $\mathrm{Ri}_c = 1$ as a threshold (no turbulence for $\mathrm{Ri} \geq 1$, increasing eddy diffusivity for decreasing Ri when $\mathrm{Ri} < 1$). However, there is no specific critical value for $\mathrm{Ri}_c$ in the free atmosphere for the WRF simulations with the YSU boundary layer scheme. The vertical diffusivity in the YSU boundary layer scheme is a sensitive function of Ri [(A18) and (A20) in Hong et al. (2006)] and qualitatively behaves in a similar way as the classic turbulent parameterization for the free atmosphere. In this section, we will first check the distribution of the Richardson number and the existence of the Richardson number criticality ($0 < \mathrm{Ri} \leq 1$) at the selected times. The Richardson number calculation used in this paper follows:

$$\mathrm{Ri} = \frac{N^2}{\mathrm{SH}^2} = \frac{\left(\frac{g}{\theta_v}\right)\left(\frac{\partial \theta_v}{\partial z}\right)}{\left(\frac{\partial V_t}{\partial z}\right)^2 + \left(\frac{\partial V_r}{\partial z}\right)^2}, \tag{4}$$

where $N$ is the Brunt–Väisälä frequency, a measure of the local static stability, $\mathrm{SH}^2$ is the squared shear magnitude, $\theta_v$ is the virtual potential temperature, $V_t$ is the azimuthally averaged tangential wind, and $V_r$ is the azimuthally averaged radial wind. The calculation is based on the local vertical gradient of $\theta_v$ and shear, which indicates that the thicker the layer/the coarser the model resolution, the more likely that large gradients will be averaged out in the small subregions of the layer of interest. Small positive Richardson number occur when the stratification is near neutral and/or when there is large vertical wind shear.

The $N^2$ distribution is shown in the first column of Fig. 6. The $N^2$ values are small just below tropopause, and values greater than $3 \times 10^{-4}\,\mathrm{s^{-2}}$ only occur in a thin layer in the TC's eye below 3-km height, which corresponds to the large positive vertical gradient of $s^*$ in

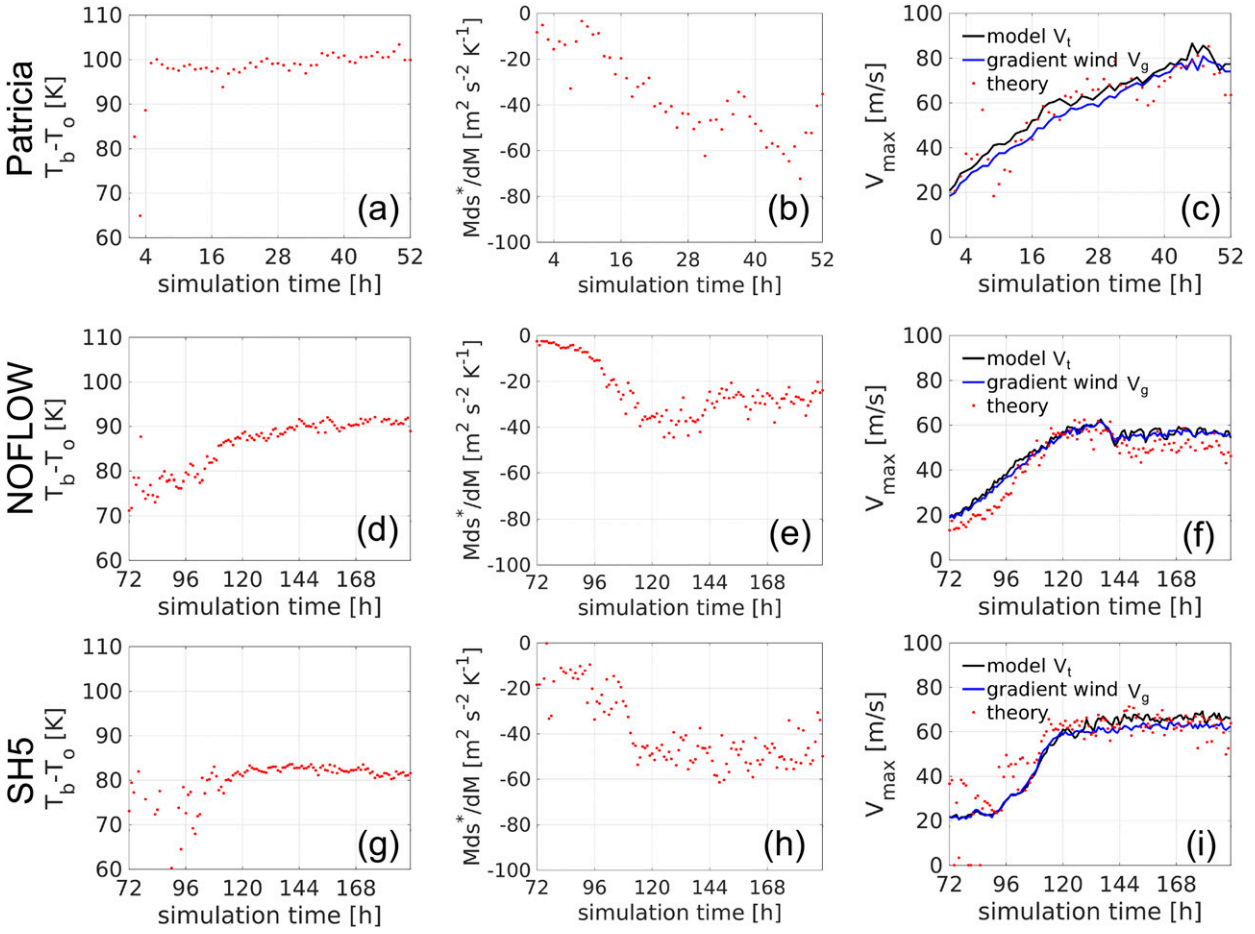


FIG. 5. (left) Temperature difference between outflow and boundary layer top. (center) Values of $M(ds^*/dM)$. (right) The black line is the modeled maximum tangential wind at the boundary layer top, the blue line is the maximum gradient wind directly deduced from modeled pressure gradient, and the red dots are the diagnosed maximum wind from (3). (a)–(c) Patricia at $z = 1.4$ km, (d)–(f) NOFLOW at $z = 1$ km, and (g)–(i) SH5 at $z = 1.5$ km.

Figs. 3a, 3c, and 3e. Above the tropopause, the $N^2$ values are large, as expected. The distributions of shear magnitudes are shown in the second column of Fig. 6. In all three cases, the shear magnitude maximizes in the boundary layer, the eyewall updrafts, and the outflow region, which is related to the structure of the TC tangential and radial flows (Fig. 2). The corresponding low Richardson numbers ($0 < \mathrm{Ri} \leq 1$) are found in the region where the eyewall updrafts intersect the outflow as well as in the boundary layer in all three cases. In NOFLOW and SH5, near-critical Richardson numbers are also found in the outflow regions extending out to radii larger than 260 km. In Patricia, the coverage of small Richardson number in the outflow region is not as large as that in NOFLOW and SH5, which is due to a coarser vertical resolution at this height as described in section 2. For a better sense of the magnitudes of $N^2$, squared shear and corresponding Richardson number, their vertical profiles at select radii are shown in Fig. 7. From the vertical profiles, we conclude that the smaller Richardson numbers in these regions are the result of both large shear and small static stability, which is consistent with the observational studies of Molinari et al. (2014) and Duran and Molinari (2016). The coarser vertical resolution of Patricia results in the smaller $\mathrm{SH}^2$ in the outflow region (Fig. 7a).

Given that the calculations of $N^2$, $\mathrm{SH}^2$ and corresponding Ri above are based on the azimuthally averaged fields and given that small-scale turbulent mixing happens locally in three dimensions, we further calculated the Richardson number at each grid point $(x, y, z)$ and then checked the occurrence of the Richardson number criticality ($0 < \mathrm{Ri} \leq 1$) along the azimuth at a given radius and height $(r, z)$. In the left column of Fig. 8, the high frequency (percentage $> 60\%$) of the Richardson number criticality in azimuth matches well with the critical Richardson number distribution

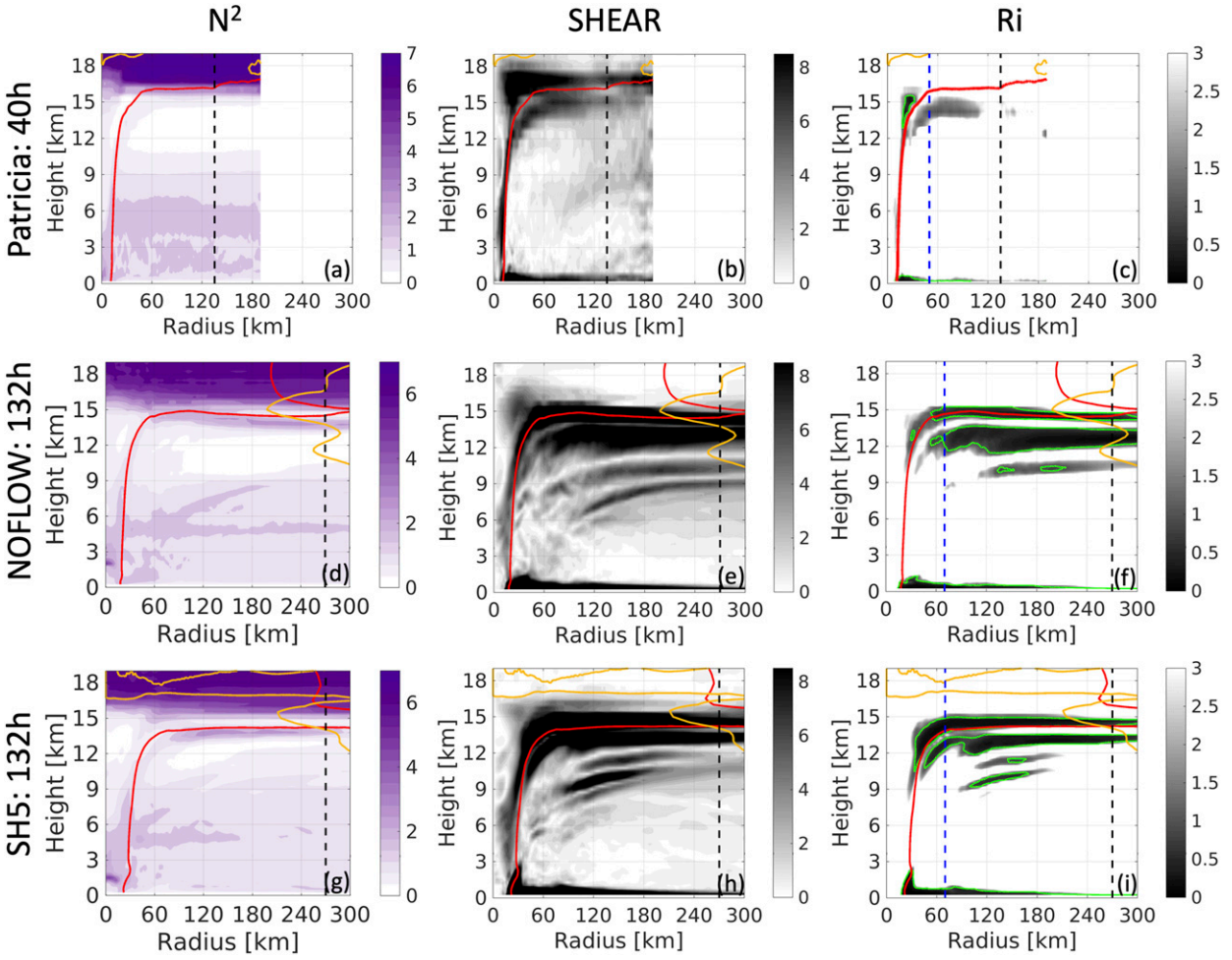


FIG. 6. (left) $N^2$ ($10^{-4}\,s^{-2}$), (center) shear ($m\,s^{-1}\,km^{-1}$), and (right) Richardson number calculated from azimuthally averaged fields for (a)–(c) Patricia at 40 h, (d)–(f) NOFLOW at 132 h, and (g),(i) SH5 at 132 h. $M_{RMW}$ is the red line, $V_t = 0\,m\,s^{-1}$ is the orange contour, and Ri = 1 is the green contour. The blue dashed lines are the locations for the profiles in Fig. 7. Black dash lines separate the area with full azimuthal data (radius ≤ 135 km in Patricia and radius ≤ 270 km in NOFLOW and SH5) and the area with partial azimuthal data (radius > 135 km in Patricia and radius > 270 km in NOFLOW and SH5).

simply using the azimuthally averaged fields (Figs. 6c,f,i). This indicates that the approximation of axisymmetry for representing the three-dimensional fields works well for TCs in a quasi-steady state.

In deriving the relationship between $M$ and Ri in ER11, the radial flow contribution to the shear is neglected. To evaluate this approximation, we calculated the ratio of $(\partial V_t/\partial z)^2$ to $[(\partial V_t/\partial z)^2 + (\partial V_r/\partial z)^2]$. A large ratio validates the assumption. The result (right column of Fig. 8) shows that the contribution of the tangential wind is dominant in the area inside the eyewall and along $M_{RMW}$ in the outflow region, while the contribution of the radial wind is dominant in the boundary layer and in the outflow region away from $M_{RMW}$. Thus, this approximation validates in the vicinity of $M_{RMW}$. Neglecting the contribution of radial wind in the shear actually leads to smaller values of $\partial T_o/\partial M$, which can result in a broader radial profile of the angular velocity above the boundary layer.

In this section, we have confirmed the Ri criticality in the outflow region near $M_{RMW}$, which indicates the existence of small-scale turbulent mixing in this area in 3D model simulations. Though there is no specific value for $Ri_c$ in the YSU boundary layer scheme, the model evolves toward a range of low but positive Ri ($0 < Ri \leq 1$) in the outflow region, in qualitative accordance with the assumption of Ri criticality in the outflow region.

### e. *Outflow temperature stratification in M coordinates*

The azimuthally averaged absolute temperature field and $M$ surfaces are shown in the left column of Fig. 9. The eye temperature inside $M_{RMW}$ is clearly higher than

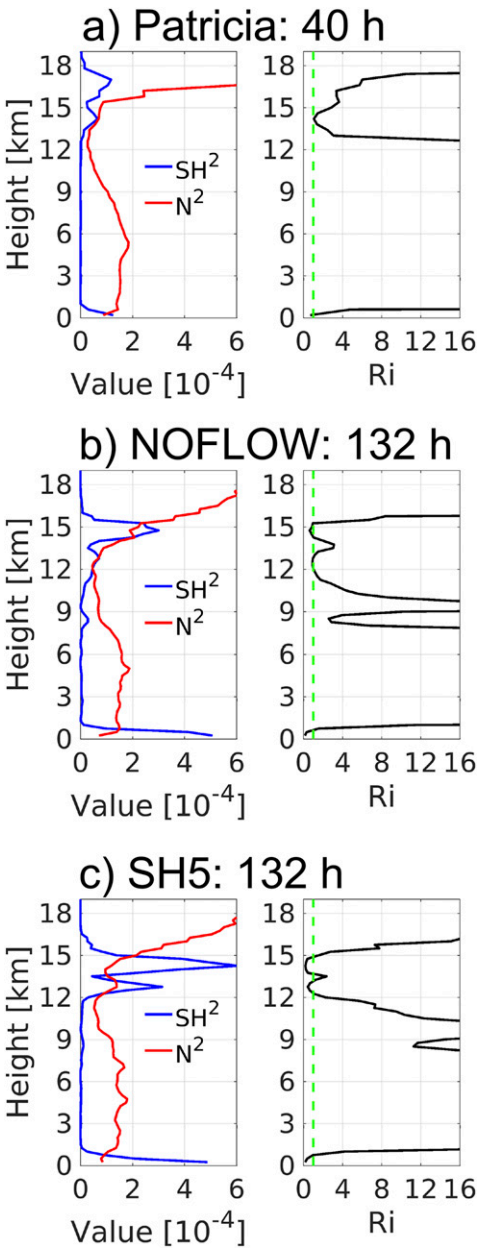


FIG. 7. Vertical profiles of (left) $N^2$ and $SH^2$ and (right) Ri at (a) $R = 50$ km in Patricia at 40 h, (b) $R = 70$ km in NOFLOW at 132 h, and (c) $R = 70$ km in SH5 at 132 h.

the temperature outside $M_{\mathrm{RMW}}$ showing the existence of warm core. The horizontal gradient of the temperature across the eyewall is considerably sharper in Patricia than those in NOFLOW and SH5, which is consistent with the smaller scale of Patricia's inner core and its higher intensity. Another interesting feature worth mentioning is the much colder tropopause temperature in Patricia, which partly contributes to its higher intensity as discussed in section 4c. The stratification of outflow temperature is quite obvious in Figs. 9a, 9d, and 9g that the $M$ surfaces in the outflow region span over a range of absolute temperature values. A clearer way to display this stratification is shown in the middle and right columns of Fig. 9, in which the $M$ surfaces calculated from azimuthally averaged tangential wind are plot as a function of azimuthally averaged tangential wind and azimuthally averaged absolute temperature. The region that this temperature stratification builds up is highlighted in the magenta box in the left panels of Fig. 9 and yellow contours of the corresponding $M$ surfaces in the right panels of Fig. 9. The magnitude of $\partial T_o/\partial M$ is largest in Patricia while Patricia has the most compact structure among the three.

Given the assumptions of gradient wind balance, hydrostatic balance and slantwise moist neutrality, the self-stratification theory proposes that the outflow temperature stratification across $M$ surfaces can be expressed by (1) in the introduction [the same as (31) in ER11]. As stated in section 4d, subcritical Richardson numbers indicate the onset/existence of small-scale turbulence. Once the flow becomes turbulent, the Richardson number should be held near a critical value. By assuming the Richardson number in the outflow is near a critical value at some physical radius $r_t$, the temperature stratification calculated by (1) at $r_t$ is then approximately used to represent the $\partial T_o/\partial M$ at $V_t = 0\,\mathrm{m\,s^{-1}}$, which acts as an upper boundary condition to derive the radial profile of gradient wind above the boundary layer. In ER11, $\mathrm{Ri}_c/r_t^2$ is replaced by

$$\frac{\mathrm{Ri}_c}{r_t^2} = \frac{C_k}{C_d}\frac{1}{r_m^2}, \tag{5}$$

where $r_m$ is the radius of maximum wind at the boundary layer top.

Following the ER11 derivation but without using (1), the outflow temperature as a function of $M$ is expressed as

$$\frac{T_o(M) - T_{\mathrm{om}}}{T_b - T_{\mathrm{om}}} = 1 - \frac{\left(\dfrac{M}{M_{\mathrm{RMW}}}\right)^{2-C_k/C_d}}{\left(\dfrac{r}{r_m}\right)^2}, \tag{6}$$

of which $T_{\mathrm{om}}$ is the outflow temperature on $M_{\mathrm{RMW}}$, $T_b$ is the boundary layer top temperature (assumed to be a constant with radius) and $T_o(M)$ is the outflow temperature on $M$. By taking $\partial/\partial M$ of (6), we get the stratification of the outflow temperature with respect to $M$ without using (1):

$$\left.\frac{\partial T_o}{\partial M}\right|_{M_{\mathrm{RMW}}} = \frac{T_b - T_{\mathrm{om}}}{M_{\mathrm{RMW}}}\left(\frac{2}{r_m}\frac{M_{\mathrm{RMW}}}{\left.\dfrac{\partial M}{\partial r}\right|_{r_m}} - 1\right), \tag{7}$$

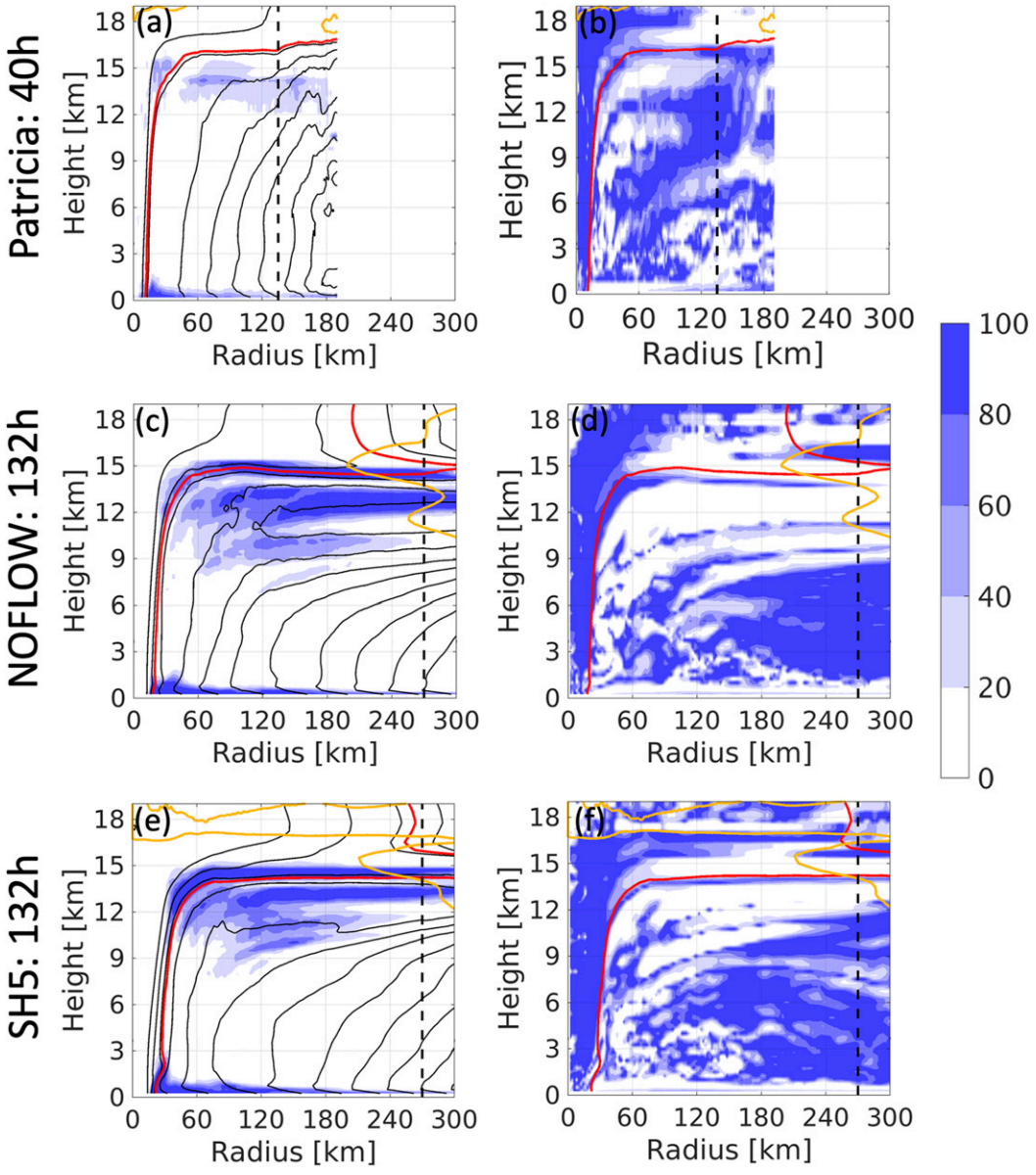


FIG. 8. (left) Percentage of $0 < \mathrm{Ri} \leq 1$ along the azimuth. (right) Ratio of $(dV_t/dz)^2/[(dV_t/dz)^2 + (dV_r/dz)^2]$. (a),(b) Patricia at 40 h, (c),(d) NOFLOW at 132 h, and (e),(f) SH5 at 132 h. The $V_t = 0\,\mathrm{m\,s^{-1}}$ contour is orange. Black dashed lines separate the area with full azimuthal data (radius $\leq$ 135 km in Patricia and radius $\leq$ 270 km in NOFLOW and SH5) and the area with partial azimuthal data (radius $>$ 135 km in Patricia and radius $>$ 270 km in NOFLOW and SH5).

where we use $C_k/C_d = 1$, $r = r_m$, and $M = M_{\mathrm{RMW}}$.

We evaluate (1) as follows: first, we use (7) to calculate the outflow temperature stratification with respect to $M$ given the radial profile of modeled tangential wind above the boundary layer (the fifth column of Table 1); second, we calculate the right-hand side of (1) using (5) and $C_k/C_d = 1$ at the boundary layer top (the last column of Table 1). The values of each term from the three simulations are listed in Table 1.

The values of $\partial T_o/\partial M$ calculated from two methods with and without (1) agree well with each other, yielding a difference less than 20%, which is equivalent to a difference in $M(r)$ of around 3% for $M$ surfaces near $M_{\mathrm{RMW}}$ [evaluated from (6)]. Therefore, (1) is approximately satisfied in the expected region, thus the self-stratification hypothesis is qualitatively consistent with the simulations of the three quasi-steady-state TC cases.

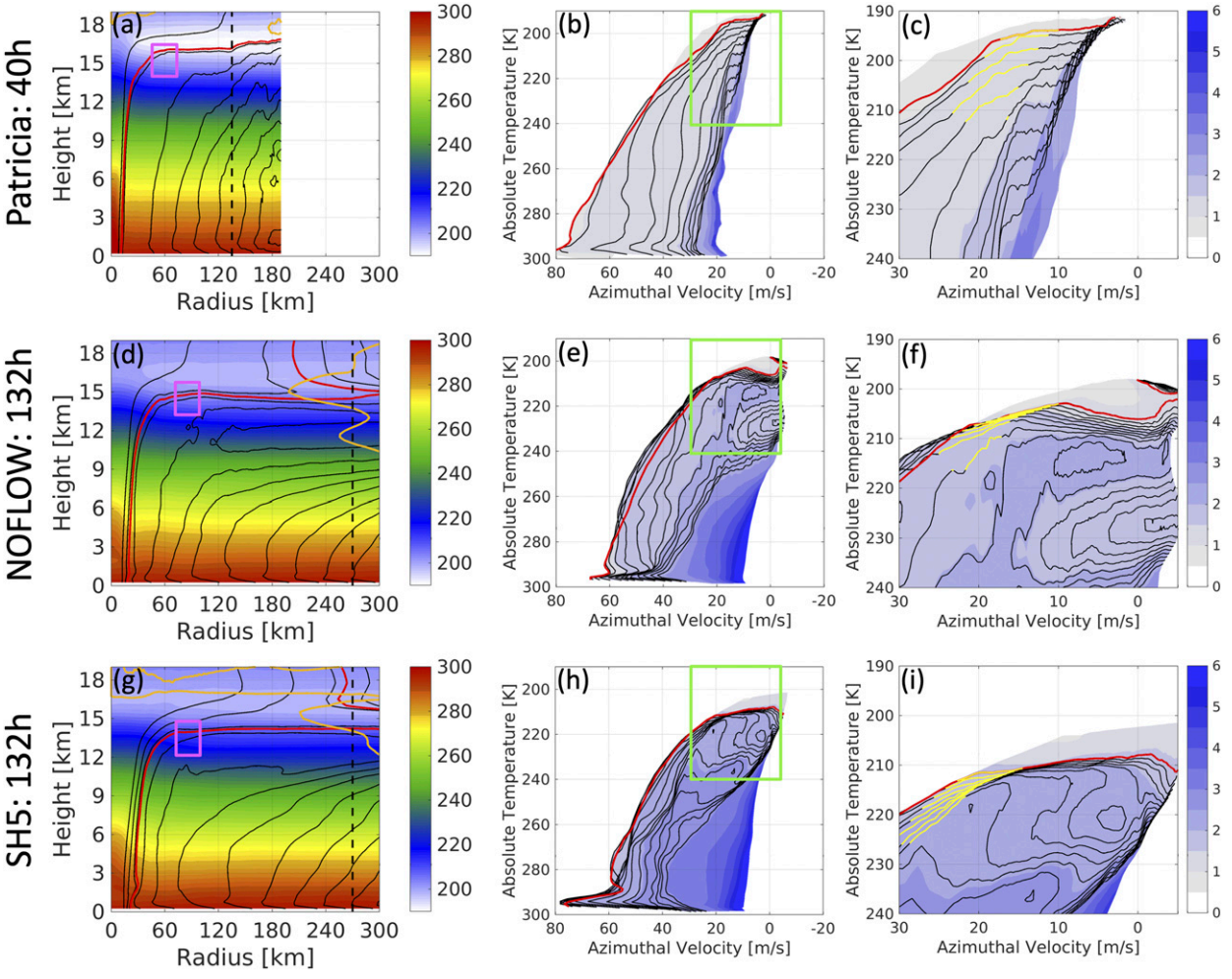


FIG. 9. (left) Azimuthally averaged temperature field (shading) and $M$ field (black contours with an interval of $0.5 \times 10^6\ \mathrm{m^2\ s^{-1}}$; $M_{\mathrm{RMW}}$ in red). The $V_t = 0\ \mathrm{m\ s^{-1}}$ contour is orange, and black dashed lines separate the area with full azimuthal data (radius $\leq$ 135 km in Patricia and radius $\leq$ 270 km in NOFLOW and SH5) and the area with partial azimuthal data (radius $>$ 135 km in Patricia and radius $>$ 270 km in NOFLOW and SH5). (center) Constant absolute angular momentum surfaces (shading; featured $M$ surfaces are contoured with an interval of $0.1 \times 10^6\ \mathrm{m^2\ s^{-1}}$) traced vs absolute temperature and azimuthal velocity. The $M_{\mathrm{RMW}}$ is in red. (right) Zoomed-in version of the green boxes in the center column. The yellow lines indicate the angular momentum inside the magenta box of the left column. (a) Patricia covering $r$ = 50–80 km and $z$ = 13.8–16.6 km, (d) NOFLOW covering $r$ = 70–100 km and $z$ = 13–16 km, and (g) SH5 covering $r$ = 70–100 km and $z$ = 12–15 km.

### *f. Radial structure of the wind at the boundary layer top*

The stratification of the outflow temperature is finally used to derive the analytical solution of the steady-state radial structure of the gradient wind at the boundary layer top in ER11. The $V(r)$ is in form of angular momentum:

$$\left(\frac{M}{M_{\mathrm{RMW}}}\right)^{2-C_k/C_d} = \frac{2\left(\frac{r}{r_m}\right)^2}{2 - \left(\frac{C_k}{C_d}\right) + \left(\frac{C_k}{C_d}\right)\left(\frac{r}{r_m}\right)^2}. \quad (8)$$

To get this analytical solution, some further assumptions are made:

1) $C_k/C_d$, $T_b$, $\mathrm{Ri}_c/r_t^2$, and sea surface saturation entropy $s_0^*$ are constants;
2) entropy and angular momentum are well mixed in the boundary layer that $ds^*/dM$ at the surface can be used to represent the $ds^*/dM$ at the boundary layer top.

Using (1) together with the gradient wind balance and slantwise moist neutrality while neglecting the Coriolis terms in the inner core and maximizing $V$ at $r_m$, we can derive the radial distribution of the gradient wind speed

TABLE 1. The outflow temperature stratification on $M$ calculated using model simulations. Column 2 is the radius of maximum wind at the top of the boundary layer (Patricia: 1.4 km; NOFLOW: 1 km; SH5: 1.5 km). Column 3 is $M_{\mathrm{RMW}}$. Column 4 is $\partial M/\partial r$ at the radius of maximum wind at the top of the boundary layer. Column 5 is the outflow temperature stratification on $M$ predicted by (7) given the radial profile of tangential wind from the simulations, and $T_b - T_{\mathrm{om}}$ is from Fig. 5. Column 6 is the right-hand side of (1) using $dM/ds^*$ in Fig. 4.

| | $r_m$ (km) | $M_{\mathrm{RMW}}$ ($10^6$ m$^2$ s$^{-1}$) | $\left.\frac{\partial M}{\partial r}\right\|_{r_m}$ (m s$^{-1}$) | $\left.\frac{\partial T_o}{\partial M}\right\|_{M_{\mathrm{RMW}}}$ ($10^{-6}$ K s m$^{-2}$) | $-\frac{1}{r_m^2}\left(\frac{dM}{ds^*}\right)$ ($10^{-6}$ K s m$^{-2}$) |
|---|---|---|---|---|---|
| Patricia | 12 | 0.91 | 62.20 | 158.06 | 132.04 |
| NOFLOW | 20 | 1.21 | 56.47 | 85.00 | 93.67 |
| SH5 | 30 | 1.96 | 62.43 | 46.29 | 44.29 |

for steady-state tropical cyclones above the boundary layer as presented in (8).

Figure 10 compares the radial profiles of model derived azimuthally averaged tangential wind speed, gradient wind speed calculated from azimuthally averaged pressure field, and analytical solution from the simplified model. The analytical solution with $C_k/C_d = 0.5$ has the broadest profile with respect to $r/r_m$. With larger $C_k/C_d$, the analytical solution becomes more compact. The radial wind profiles of Patricia and SH5 derived from the model simulations tend to be more compact than the analytical solutions with $C_k/C_d$ in a reasonable range of [0.5, 1.5] (Bell et al. 2012) inside ~6RMW. The radial profile of the tangential wind in NOFLOW outside RMW decays more slowly than that in Patricia and SH5, which is closer to the analytical solution. This, however, is due to the broadening of the wind field before the secondary eyewall formation (secondary updrafts near 40-km radius shown in Fig. 2d) in NOFLOW.

The discrepancies in the profiles are not surprising in view of the assumptions to derive the analytical solution. First of all, $C_k/C_d$ in the model is not constant with radius (decreasing with radius outside the eyewall region in these simulations). Second, the assumption that the boundary layer is well mixed, which is however not the case as shown in many studies (J. A. Zhang et al. 2011; Kepert et al. 2016), will introduce some deviation of the analytical solution from the modeled $ds^*/dM$ and hence the radial profile. Third, the three-dimensional simulations have an additional dimension of freedom compared to axisymmetric models, permitting asymmetries at all scales that can have an impact on the distribution of surface fluxes and stress (hence $s^*$ and $M$ in the boundary layer) as well as the storm structure. Besides the discrepancies in the parameters, neglecting the radial component of the vertical shear in the derivation of ER11 and the gradient of temperature with respect to $s^*$ in pressure coordinates [first term on the right-hand side of (29) in ER11] will lead to smaller $\partial T_o/\partial M$. Given the smaller $\partial T_o/\partial M$ used in the analytic solution, the radial profile of angular velocity can be expected to be broader than the modeled radial profile. Nevertheless, the analytical solution and its derivation process are beneficial for understanding tropical cyclones from both the dynamic and thermodynamic aspects as well as giving insights on the connection of the outflow region and the boundary layer dynamics. Generally speaking, the analytical solution gives a plausible approximate radial profile for the tangential wind above the boundary layer for mature tropical cyclones.

## 5. Summary and conclusions

Three simulations (one deterministic forecast of Hurricane Patricia, one idealized case with no background flow, and one idealized case with vertical wind shear) are used to evaluate the assumptions used in ER11, the diagnosed maximum gradient wind at the boundary layer top and the analytical solution of the radial profile for gradient wind above the boundary layer. The three cases are representative of three groups of TCs: real TCs with asymmetries and strong environmental influences, TCs in idealized homogeneous environment with near-axisymmetric structures, and TCs in idealized sheared environments with asymmetries.

The diagnosed maximum gradient wind at the boundary layer top using (3) is quantitatively comparable to the modeled maximum azimuthally averaged tangential wind and gradient wind calculated from the azimuthally averaged pressure field after an initial organization stage, when the congruence of $s^*$ and $M$ surfaces becomes established, as shown by Peng et al. (2018). One important thing to emphasize is that the diagnosed maximum $V$ from (3) is for the gradient wind, while the model simulated flow can be supergradient within the boundary layer. For the three cases in this study, the diagnosed maximum $V$ is consistently smaller than the modeled maximum tangential wind $V_t$ but comparable to the maximum gradient wind $V_g$ within the boundary layer, as expected (Figs. 2c,f,i).

In the three cases studied in this paper, the slantwise moist neutrality assumption is satisfied along the $M_{\mathrm{RMW}}$ surface from the boundary layer top through the outflow region. Near-critical Richardson numbers are found in

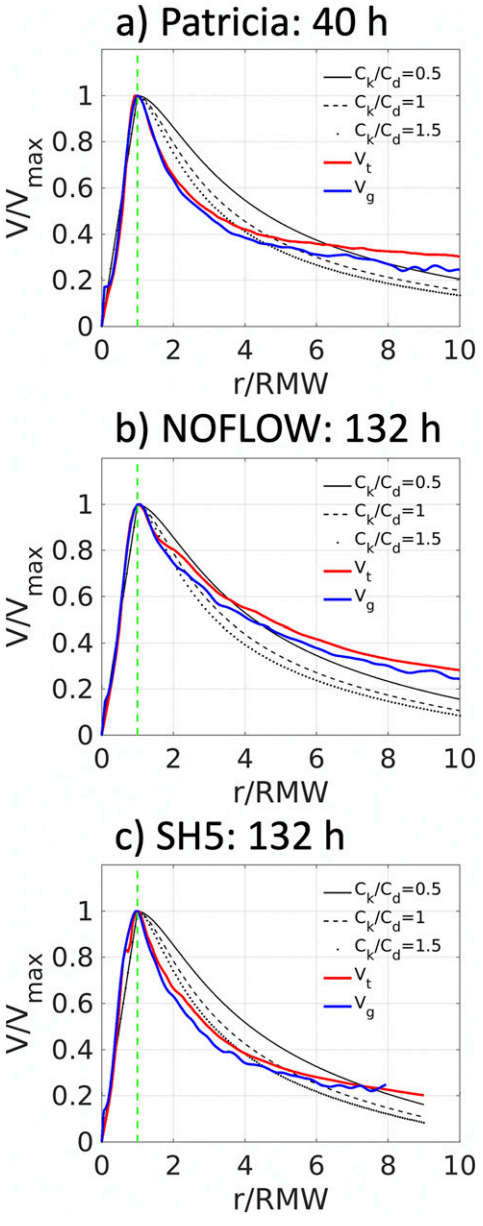


FIG. 10. Radial profiles of the analytic solutions from the steady-state ER11 model with $C_k/C_d = 0.5$, 1, and 1.5 and radial profiles of the azimuthally averaged tangential wind and gradient wind at the boundary layer top. (a) Patricia at $z = 1.4$ km, (b) NOFLOW at $z = 1$ km, and (c) SH5 at $z = 1.5$ km.

the outflow region along $M_{\mathrm{RMW}}$, resulting from the large vertical wind shear and the reasonably small Brunt–Väisälä frequency in the upper troposphere. The criticality of Richardson numbers in the outflow region indicates the existence of small-scale turbulent mixing. We also analyzed several simulations with the same setups but different vertical and horizontal grid spacings (not shown), and found that the degree of Richardson number criticality in the outflow region is closely related to the model resolutions, especially the vertical resolution. The higher model resolution (mainly vertical), the larger the area of Richardson number criticality. However, the region where the updrafts transition to the outflow always has small Richardson number.

The results of this analysis support the hypothesis of ER11 and E12 that the intensity and structure of tropical cyclones partially depend on the stratification of the outflow temperature. Equation (1) gives a plausible estimate of the outflow temperature stratification on $M$ surfaces at $V_t = 0\,\mathrm{m\,s^{-1}}$, which is used to further derive (8). The analyses in sections 4a–4e also work for developing storms with established slantwise neutrality, while the analytical solution given by (8) is for steady-state tropical cyclones (steady-state assumption is used during derivation). The simulated radial structure of tangential wind at the boundary layer top is broadly consistent with the analytic solution based on the assumption of criticality in the outflow region, but there are some discrepancies due to simplifications in the analytic model as described in section 4f. Further analysis of how the outflow temperature stratification evolves and analysis of the theoretical assumptions in the boundary layer will be studied in follow-up research.

*Acknowledgments.* Authors Tao and Zhang were partially supported by NSF Grant AGS-1305798, ONR Grant N000140910526, and NOAA HFIP. Robert Nystrom was supported by NASA Grant 17-EARTH17F-184. Kerry Emanuel was supported by the Office of Naval Research under Grant ONR N00014-18-1-2458. The contribution of R. Rotunno to this work is supported by the National Center for Atmospheric Research, which is a major facility sponsored by the National Science Foundation under Cooperative Agreement 1852977. Michael Bell was supported by ONR Grant N000141613033 and NSF Grant AGS-1701225. Computing was performed at the Texas Advanced Computer Center.

## REFERENCES

Bell, M. M., M. T. Montgomery, and K. A. Emanuel, 2012: Air–sea enthalpy and momentum exchange at major hurricane wind speeds observed during CBLAST. *J. Atmos. Sci.*, **69**, 3197–3222, https://doi.org/10.1175/JAS-D-11-0276.1.

Chen, Y., and X. Yu, 2016: Enhancement of wind stress evaluation method under storm conditions. *Climate Dyn.*, **47**, 3833–3843, https://doi.org/10.1007/s00382-016-3044-4.

——, F. Zhang, B. W. Green, and Y. Xu, 2018: Impacts of ocean cooling and reduced wind drag on Hurricane Katrina (2005) based on numerical simulations. *Mon. Wea. Rev.*, **146**, 287–306, https://doi.org/10.1175/MWR-D-17-0170.1.

Cohen, Y., N. Harnik, E. Heifetz, D. S. Nolan, D. Tao, and F. Zhang, 2017: On the violation of gradient wind balance at the top of tropical cyclones. *Geophys. Res. Lett.*, **44**, 8017–8026, https://doi.org/10.1002/2017GL074552.

Dunion, J. D., 2011: Rewriting the climatology of the tropical North Atlantic and Caribbean Sea. *J. Climate*, **24**, 893–908, https://doi.org/10.1175/2010JCLI3496.1.

Duran, P., and J. Molinari, 2016: Upper-tropospheric low Richardson number in tropical cyclones: Sensitivity to cyclone intensity and the diurnal cycle. *J. Atmos. Sci.*, **73**, 545–554, https://doi.org/10.1175/JAS-D-15-0118.1.

Emanuel, K. A., 1986: An air–sea interaction theory for tropical cyclones. Part I: Steady-state maintenance. *J. Atmos. Sci.*, **43**, 585–604, https://doi.org/10.1175/1520-0469(1986)043<0585:AASITF>2.0.CO;2.

——, 1997: Some aspects of hurricane inner-core dynamics and energetics. *J. Atmos. Sci.*, **54**, 1014–1026, https://doi.org/10.1175/1520-0469(1997)054<1014:SAOHIC>2.0.CO;2.

——, 2012: Self-stratification of tropical cyclone outflow. Part II: Implications for storm intensification. *J. Atmos. Sci.*, **69**, 988–996, https://doi.org/10.1175/JAS-D-11-0177.1.

——, and R. Rotunno, 2011: Self-stratification of tropical cyclone outflow. Part I: Implications for storm structure. *J. Atmos. Sci.*, **68**, 2236–2249, https://doi.org/10.1175/JAS-D-10-05024.1.

Hong, S.-Y., and J.-O. J. Lim, 2006: The WRF single-moment 6-class microphysics scheme (WSM6). *J. Korean Meteor. Soc.*, **42**, 129–151.

——, Y. Noh, and J. Dudhia, 2006: A new vertical diffusion package with an explicit treatment of entrainment processes. *Mon. Wea. Rev.*, **134**, 2318–2341, https://doi.org/10.1175/MWR3199.1.

Kepert, J. D., J. Schwendike, and H. Ramsay, 2016: Why is the tropical cyclone boundary layer not "well mixed"? *J. Atmos. Sci.*, **73**, 957–973, https://doi.org/10.1175/JAS-D-15-0216.1.

Molinari, J., P. Duran, and D. Vollaro, 2014: Low Richardson number in the tropical cyclone outflow layer. *J. Atmos. Sci.*, **71**, 3164–3179, https://doi.org/10.1175/JAS-D-14-0005.1.

Nolan, D. S., 2011: Evaluating environmental favorableness for tropical cyclone development with the method of point downscaling. *J. Adv. Model. Earth Syst.*, **3**, M08001, https://doi.org/10.1029/2011MS000063.

Peng, K., R. Rotunno, and G. H. Bryan, 2018: Evaluation of a time-dependent model for the intensification of tropical cyclones. *J. Atmos. Sci.*, **75**, 2125–2138, https://doi.org/10.1175/JAS-D-17-0382.1.

——, ——, ——, and J. Fang, 2019: Evolution of an axisymmetric tropical cyclone before reaching slantwise moist neutrality. *J. Atmos. Sci.*, **76**, 1865–1884, https://doi.org/10.1175/JAS-D-18-0264.1.

Rogers, R. F., and Coauthors, 2017: Rewriting the tropical record books: The extraordinary intensification of Hurricane Patricia (2015). *Bull. Amer. Meteor. Soc.*, **98**, 2091–2112, https://doi.org/10.1175/BAMS-D-16-0039.1.

Tao, D., and F. Zhang, 2014: Effect of environmental shear, sea-surface temperature, and ambient moisture on the formation and predictability of tropical cyclones: An ensemble-mean perspective. *J. Adv. Model. Earth Syst.*, **6**, 384–404, https://doi.org/10.1002/2014MS000314.

——, and ——, 2019: Evolution of dynamic and thermodynamic structures before and during rapid intensification of tropical cyclones: Sensitivity to vertical wind shear. *Mon. Wea. Rev.*, **147**, 1171–1191, https://doi.org/10.1175/MWR-D-18-0173.1.

Weng, Y., and F. Zhang, 2016: Advances in convection-permitting tropical cyclone analysis and prediction through EnKF assimilation of reconnaissance aircraft observations. *J. Meteor. Soc. Japan*, **94**, 345–358, https://doi.org/10.2151/jmsj.2016-018.

Willoughby, T. M., 1979: Forced secondary circulations in hurricanes. *J. Geophys. Res.*, **84**, 3173–3183, https://doi.org/10.1029/JC084iC06p03173.

Zhang, F., and Y. Weng, 2015: Predicting hurricane intensity and associated hazards: A five-year real-time forecast experiment with assimilation of airborne Doppler radar observations. *Bull. Amer. Meteor. Soc.*, **96**, 25–32, https://doi.org/10.1175/BAMS-D-13-00231.1.

——, ——, J. A. Sippel, Z. Meng, and C. H. Bishop, 2009: Cloud-resolving hurricane initialization and prediction through assimilation of Doppler radar observations with an ensemble Kalman filter: Humberto (2007). *Mon. Wea. Rev.*, **137**, 2105–2125, https://doi.org/10.1175/2009MWR2645.1.

——, ——, J. F. Gamache, and F. D. Marks, 2011: Performance of convection-permitting hurricane initialization and prediction during 2008–2010 with ensemble data assimilation of inner-core airborne Doppler radar observations. *Geophys. Res. Lett.*, **38**, L15810, https://doi.org/10.1029/2011GL048469.

Zhang, J. A., R. F. Rogers, D. S. Nolan, J. Marks, and D. Frank, 2011: On the characteristic height scales of the hurricane boundary layer. *Mon. Wea. Rev.*, **139**, 2523–2535, https://doi.org/10.1175/MWR-D-10-05017.1.